Electronic transport in titanium carbide MXenes from first principles

Nesrine Boussadoune, Olivier Nadeau, and Gabriel Antonius[*]

Département de Chimie, Biochimie et Physique, Institut de recherche sur l'hydrogène,
Université du Québec à Trois-Rivières, Trois-Rivières, Canada

We compute from first principles the electronic, vibrational, and transport properties of four known MXenes: Ti_3C_2, $Ti_3C_2F_2$, $Ti_3C_2(OH)_2$, and Ti_2CF_2. We study the effect of different surface terminations and monosheet thickness on the electrical conductivity, and show that the changes in conductivity can be explained by the squared velocity density of the electronic state, as well as their phonon scattering lifetime. We also compare the solution of the iterative Boltzmann transport equation (IBTE) to different linearized solutions, namely, the self-energy relaxation time approximation (SERTA) and the momentum relaxation time approximation (MRTA), and we show that the SERTA significantly underestimates the electrical conductivity while the MRTA yields results in better agreement with the IBTE. The computed monolayer conductivity at 300 K is in reasonable agreement with reported experimental measurements.

I. INTRODUCTION

MXenes form a large family of two-dimensional transition metal carbides and nitrides with interesting electrochemical properties [1–7]. These layered materials have shown potential for a wide range of applications in energy storage and conversion [8–13]. Their high specific surface area and electrochemical activity make them suitable for supercapacitors [9,13–16], lithium-ion batteries [17–19], catalysis [20], photocatalysis [21,22], and hydrogen storage [23,24]. With a suitable hydrophilic surface termination, MXenes also exhibit electrocatalytic activity for the oxygen evolution reaction (OER) [22,25], the oxygen reduction reaction (ORR) [26], and the hydrogen evolution reaction (HER) [27,28].

The terminated MXenes have a general chemical formula $M_{n+1}X_nT_x$ ($n = 1$, 2, or 3), where M is a transition metal (Sc, Ti, Zr, Hf, V, Nb, Ta, Cr, Mo, etc.); X denotes carbon and/or nitrogen; T represents the surface terminations group, typically -O, -OH or -F [9,29,30]; and x is the number of terminations. The surface termination of the two-dimensional (2D) layers originates from their synthesis by chemical etching [17,31–33], starting from three-dimensional precursors known as MAX phases [29,34], of which nearly 100 compounds have been identified [1,2,35–37]. Previous first-principles calculations have investigated how the surface termination alters the electronic properties of the MXenes [3,17,38,39]. Some MXenes become semiconductors when terminated by oxygen, such as Ti_2CO_2, Zr_2CO_2, and Hf_2CO_2 [40], while others, like V_2C, remain metallic for all surface terminations [41].

Beyond their general classification as metals or semiconductors, a key property of these materials for most applications is their electrical conductivity. The electronic transport properties can be computed from first principles within the framework of the Boltzmann transport equation (BTE), assuming that phonon scattering is the dominant scattering mechanism at room temperature and above, and neglecting other scattering channels such as defects and impurities [42]. Furthermore, one avoids solving the BTE iteratively (IBTE) by using the self-energy relaxation time approximation (SERTA) or the momentum relaxation time approximation (MRTA) [43–45]. This framework has been widely used to study the electrical transport semiconductors and metals [44–49]. It has been recently shown, however, that some of these approximations may underestimate significantly the charge mobility in semiconductors, while the IBTE can be achieved at virtually the same computational cost [50].

In the present work, we study the phonon-limited electrical conductivity of four MXenes: Ti_3C_2, $Ti_3C_2F_2$, $Ti_3C_2(OH)_2$, and Ti_2CF_2. The choice of these MXenes is motivated by the availability of experimental data for the conductivity of $Ti_3C_2(OH)_2$ and $Ti_3C_2F_2$ [6,7,37,51–67], while the comparison with Ti_3C_2 and $Ti_2C_{F_2}$ allows us to discern the influence of surface termination and monosheet thickness on the scattering lifetime of the charge carriers. We also compare the different frameworks for computing the electrical conductivity, and find that the conclusions of Claes *et al.* [50] do hold for this class of two-dimensional metallic systems, namely, that the SERTA approach underestimates the electrical conductivity while the MRTA results are in better agreement with the IBTE. We show that the predicted conductivity is consistent with experimental measurements.

II. RESULTS AND DISCUSSION

A. Computational details

We perform density functional theory (DFT) and density functional perturbation theory (DFPT) calculations using the ABINIT software [68,69] to obtain the structural, electronic, and vibrational properties of the materials. We use the Perdew-Burke-Ernzerhof (PBE) exchange-correlation

*gabriel.antonius@uqtr.ca

TABLE I. Lattice parameters, fractional atom coordinates, and bond lengths obtained from structural optimization.

Material	Lattice parameters (Å)	Atomic positions	Bond lengths (Å)
Ti$_3$C$_2$	3.098	Ti (0, 0, 0.5) Ti (1/3, 2/3, 0.6227) C (1/3, 2/3, 0.4307)	Ti1-C 2.056 Ti2-C 2.219
Ti$_3$C$_2$F$_2$	3.076	Ti (0, 0, 0.5) Ti (1/3, 2/3, 0.5934) C (1/3, 2/3, 0.4491) F (0, 0, 0.3573)	Ti1-C 2.077 Ti2-C 2.1952 Ti1-F 2.171
Ti$_3$C$_2$(OH)$_2$	3.086	Ti (0, 0, 0.5) Ti (1/3, 2/3, 0.6278) C (1/3, 2/3, 0.4309) O (0, 0, 0.3039) H (0, 0, 0.2518)	Ti1-C 2.088 Ti2-C 2.195 Ti1-O 2.186
Ti$_2$CF$_2$	3.0587	Ti (1/3, 2/3, 0.3994) Ti (2/3, 1/3, 0.4756) C (1, 1, 0.4375) F (1, 1, 0.5171)	Ti1-C 2.1032 Ti1-F 2.162

functional [70], with norm-conserving pseudopotentials from the PSEUDO-DOJO database [71]. For all the structures considered, we use an energy cutoff of 35 Hartree to represent the wave functions, and a $16\times16\times1$ **k**-points grid to sample the Brillouin zone when computing the ground state density, such that the energy is converged within 10^{-6} eV/cell.

B. Structural parameters

All the 2D materials considered assume the space group $P6_3/mmc$. We perform geometry optimization to relax the forces below 10^{-5} eV/Å. The resulting lattice parameters, atomic positions, and bond lengths are presented in Table I. These structural parameters agree very well with those of previous calculations [72,73]. The cell parameter in the z direction is set to 20 Å, allowing for a vacuum distance of at least 15 Å to avoid interactions between the periodic images of the monolayers. Several possible configurations exist for the surface termination of $Ti_{n+1}C_nT_x$ [30,72,74]. We use the most energetically favorable configuration where surface termination atoms (F or OH) are at the hollow site of three neighboring carbon atoms.

C. Electronic bands

The band structure and the PDOS of the materials are presented in Figs. 1(e)–1(h). The PDOS is obtained by projecting the electronic orbitals on the angular momentum of the last valence orbital (s for H; p for C, O, and F; d for Ti), in a sphere defined by the pseudopotential radius. All the materials are metallic, with the electronic states near the Fermi level mostly composed of Ti d orbitals. For the surface-terminated systems, the band in the $M–K$ direction is highly dispersive at the Fermi level, suggesting a high electrical conductivity [75]. We note the presence of a valley and a flat band region along the $\Gamma–K$ direction, which contribute to singularities in the density of states and represent potential scattering channels for the charge carriers.

D. Phonon bands

In Figs. 1(i)–1(l), we present the phonon band structures and the projected phonon density of states. These results were obtained by employing a coarse **q**-points mesh of $8\times8\times1$ for Ti$_3$C$_2$, Ti$_3$C$_2$F$_2$, and T_3C$_2$(OH)$_2$, and $16\times16\times1$ for Ti$_2$CF$_2$. Every phonon frequency is real and positive, indicating that the structures are stable with respect to atomic displacements [76,77].

From the projected phonon density of states, we see a clear energy separation between the phonon modes associated with the different atomic species. The low-frequency bands correspond to the vibrating motion of the metallic atoms, the high-frequency bands are associated with the motion of carbon atoms, and the surface terminations bring additional phonon bands at intermediate energies. This general feature has been observed in other MXene materials as well [10,41].

E. Electrical conductivity

The electrical conductivity can be computed by solving the IBTE where the main scattering mechanism are the phonon collisions, which are described by the electron-phonon coupling matrix elements computed from first principles [45,78]. By making use of the relaxation time approximation, the BTE can be linearized, avoiding the iterative procedure and writing the electrical conductivity σ_α as

$$\sigma_\alpha = \frac{-e}{\Omega} \sum_n \int \frac{d\mathbf{k}}{\Omega_{BZ}} \tau_{n\mathbf{k}}(T) |v_{n\mathbf{k}\alpha}|^2 f'(\varepsilon_{n\mathbf{k}}), \qquad (1)$$

where α is a Cartesian direction, Ω is the volume of the unit cell, Ω_{BZ} is the volume of the Brillouin zone, $\tau_{n\mathbf{k}}(T)$ is the temperature-dependent scattering lifetimes of the electron state, $v_{n\mathbf{k}\alpha}$ is the electron velocity, and $f'(\varepsilon)$ is the derivative of the Fermi-Dirac distribution, which depends on temperature. Different approximations exist for the computation of the electron scattering lifetime, including the SERTA [44,45] and the MRTA [46,50]. In the SERTA, the inverse lifetime is proportional to the imaginary part of the Fan-Migdal
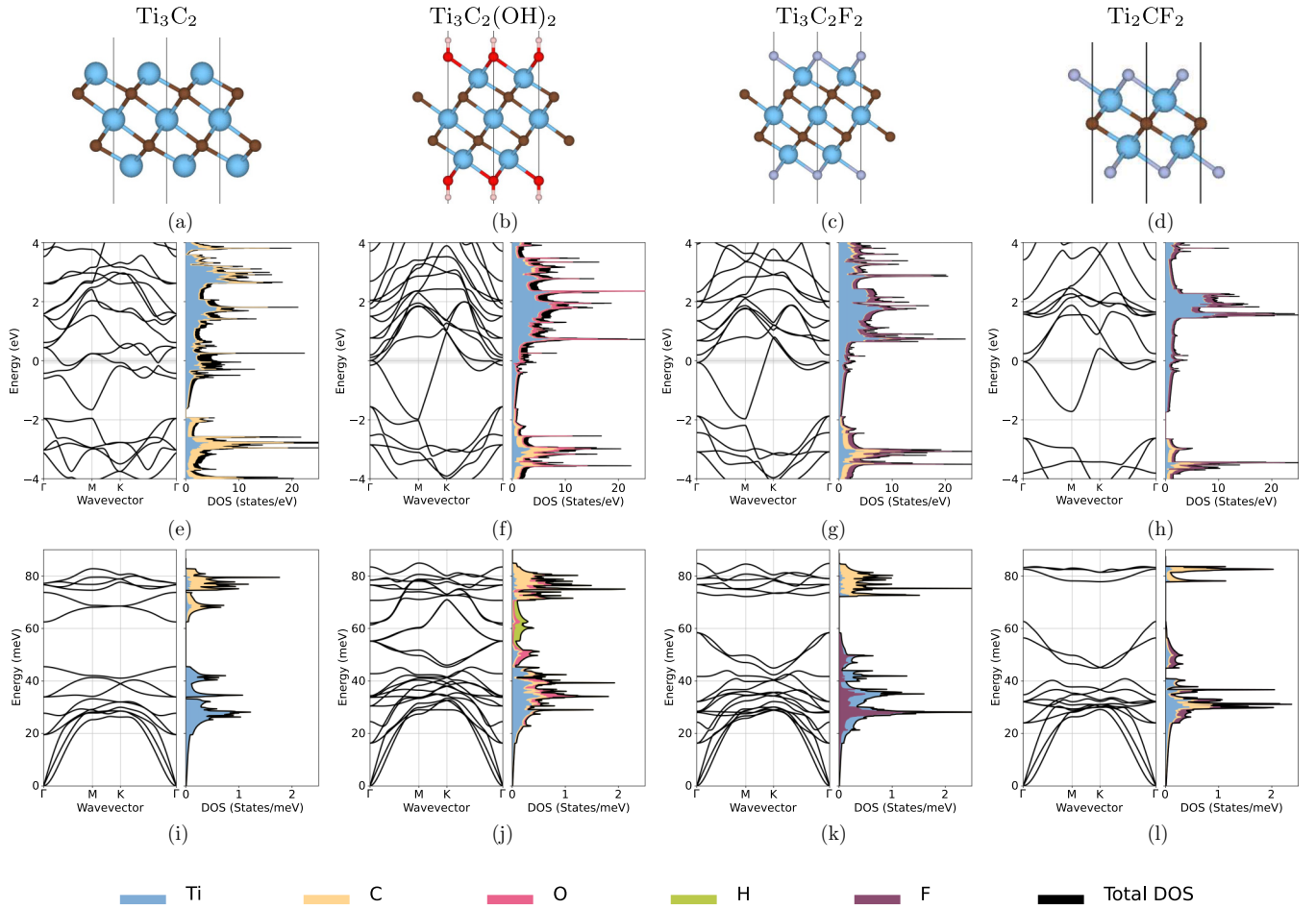
FIG. 1. (a)–(d) Structure of the monosheet materials. Titanium atoms are in blue, carbon in brown, fluorine in gray, oxygen in red, and hydrogen in pink. (e)–(h) Electronic band structures along the high symmetry directions and projected density of states (PDOS). The energy levels are referenced to the Fermi level at zero. (i)–(l) Phonon band structures along the high symmetry directions and projected phonon density of states. Note that $Ti_3C_2(OH)_2$ also possess two phonon branches associated with the motion of the hydrogen atoms at an energy of 449 meV.

self-energy:

$$\tau_{n\mathbf{k}}^{-1} = 2\pi \sum_{m\nu} \int \frac{d\mathbf{q}}{\Omega_{BZ}} |g_{mn\nu}(\mathbf{k}, \mathbf{q})|^2 P(\epsilon_{n\mathbf{k}}, \epsilon_{m\mathbf{k}+\mathbf{q}}, \omega_{\mathbf{q}\nu}, T)$$

(2)

with

$$P(\epsilon_{n\mathbf{k}}, \epsilon_{m\mathbf{k}+\mathbf{q}}, \omega_{\mathbf{q}\nu}, T)$$
$$= \left(1 - f_{m\mathbf{k}+\mathbf{q}}^0 + n_{\mathbf{q}\nu}\right)\delta\left(\epsilon_{n\mathbf{k}} - \epsilon_{m\mathbf{k}+\mathbf{q}} - \hbar\omega_{\mathbf{q}\nu}\right)$$
$$+ \left(f_{m\mathbf{k}+\mathbf{q}}^0 + n_{\mathbf{q}\nu}\right)\delta\left(\epsilon_{n\mathbf{k}} - \epsilon_{m\mathbf{k}+\mathbf{q}} + \hbar\omega_{\mathbf{q}\nu}\right).$$

(3)

Here, $g_{mn\nu}(\mathbf{k}, \mathbf{q})$ is the electron-phonon coupling matrix element, m is an electron state with energy $\epsilon_{m\mathbf{k}+\mathbf{q}}$ and Fermi-Dirac occupation number $f_{m\mathbf{k}+\mathbf{q}}^0$, and ν is a phonon mode with energy $\hbar\omega_{\mathbf{q}\nu}$ and Bose-Einstein occupation number $n_{\mathbf{q}\nu}$. The MRTA attempts to better describe the solution of the IBTE by adding an efficiency factor to each electron-phonon scattering event, writing [50]

$$\tau_{n\mathbf{k}}^{-1} = 2\pi \sum_{m\nu} \int \frac{d\mathbf{q}}{\Omega_{BZ}} |g_{mn\nu}(\mathbf{k}, \mathbf{q})|^2 \alpha_{mn}^{\mathrm{MRTA}}(\mathbf{k}, \mathbf{q})$$
$$\times P(\epsilon_{n\mathbf{k}}, \epsilon_{m\mathbf{k}+\mathbf{q}}, \omega_{\mathbf{q}\nu}, T),$$

(4)

where the efficiency factor

$$\alpha_{mn}^{\mathrm{MRTA}}(\mathbf{k}, \mathbf{q}) = \left(1 - \frac{\mathbf{v}_{n\mathbf{k}} \cdot \mathbf{v}_{m\mathbf{k}+\mathbf{q}}}{|\mathbf{v}_{n\mathbf{k}}|^2}\right)$$

(5)

accounts for the momentum direction of the final scattering state relative to the initial one.

F. Convergence study

One of the main challenges in computing the electrical conductivity is the fine sampling of electron (**k**-point) and phonon (**q**-point) wave vectors required to converge the transport properties [69,79]. A dense **k**-mesh is required to achieve good sampling of the electronic states near the Fermi level, while a dense **q**-sampling is required to converge the electronic lifetimes [79]. This is especially true in two-dimensional metals, where the density of states is expected to vary rapidly near the Fermi level, as can be seen in Figs. 1(e)–1(h).

In order to optimize the overall computational cost, we employ the Shankland-Koelling-Wood interpolation scheme [80,81], a feature recently made available within the ABINIT automated work flows [48,69]. The electronic energies and
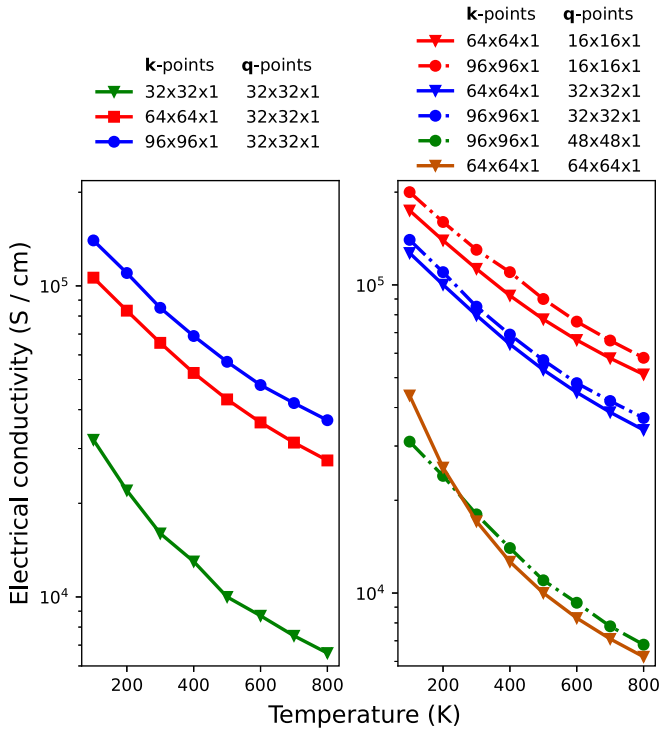
FIG. 2. Convergence of the electrical conductivity in Ti$_3$C$_2$F$_2$ with respect to the Brillouin zone sampling of electron (**k**) and phonon (**q**) wave vectors. Left: Varying **k**-point grids and fixed **q**-point grid. Right: Varying **q**-point grids and commensurate **k**-point grids.

wave functions near the Fermi level are interpolated from a coarse **k**-grid onto a fine **k**-grid. We set the coarse **k**-grid to 16×16×1 and vary the fine **k**-grid to perform the convergence study.

Figure 2 shows the convergence of the temperature-dependent electrical conductivity of Ti$_3$C$_2$F$_2$ with varying **k**-point and **q**-point grids. From this figure, we conclude that a 64×64×1 homogeneous grid for both **k**-points and **q**-points is sufficiently converged, and we use these parameters for all the studied materials. By comparing the two most converged curves (green and brown on the graph to the right), we estimate that the precision on the conductivity at 300 K and above is better than 10%.

G. Results for the electrical conductivity

The temperature-dependent electrical conductivity of the four MXenes with different approximations is presented in Fig. 3. We note, again, that the IBTE calculation uses the same computational cost as the SERTA and MRTA calculations. We find that the SERTA underestimates the conductivity by as much as 14% at $T = 300$ K and 4% at $T = 800$ K, compared to the IBTE, while the MRTA is in somewhat better agreement with the IBTE (9% at $T = 300$ K and 0.8% at $T = 800$ K).

In Fig. 4, we decompose the SERTA electrical conductivity into functions separating the integrants of Eq. (1). The derivative of the equilibrium Fermi-Dirac distribution function $-\frac{\partial f}{\partial \varepsilon}$ is peaked around the Fermi level and indicates the
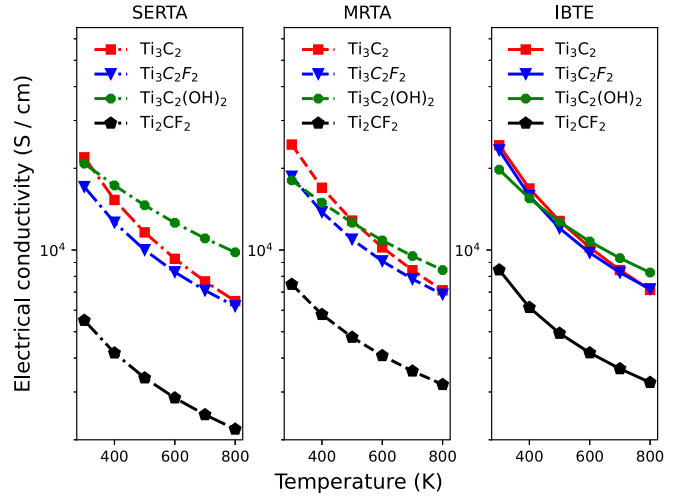

FIG. 3. Temperature-dependent electrical conductivity of each structures with the linearized (SERTA, MRTA) and iterative Boltzmann transport equation (IBTE).

energy range where the electronic states may contribute to the conductivity at a certain temperature. The squared velocity density $\langle v^2 \rangle$ is defined as

$$\left\langle v_\alpha^2 (\varepsilon) \right\rangle = \sum_n \int \frac{d\mathbf{k}}{\Omega_{Bz}} |v_{n\mathbf{k}\alpha}|^2 \, \delta(\varepsilon - \varepsilon_{n\mathbf{k}}). \quad (6)$$

This function is temperature independent and indicates both the number of carriers available at a certain energy and their squared velocity. It is a smooth function of energy, unlike the density of states, which, for 2D materials, has a spiky
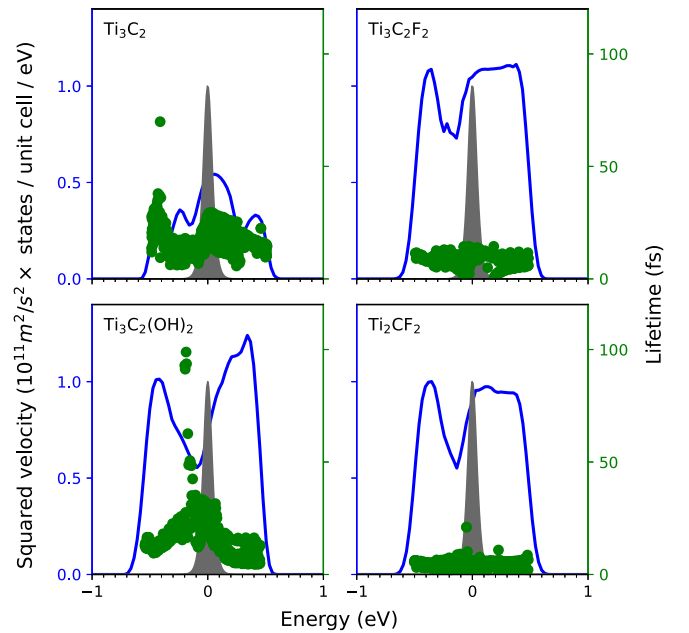

FIG. 4. The phonon self-energy lifetime at $T = 300$ K of each electronic state near the Fermi level (green disks) and the squared velocity density (blue) with $\alpha = 1$, that is, the direction along a primitive vector. The gray shaded curve represents the negative of the derivative of the Fermi-Dirac distribution.

TABLE II. Measured and computed electrical conductivity at 300 K: bulk conductivity (σ), interlayer distance (L_z), monolayer conductivity (σ_{2D}).

Material	σ (10^3 S cm^{-1})	L_z (Å)	σ_{2D} (10^{-3} S)	Reference
$Ti_3C_2T_x$	24.0	12.34	2.96	[64]
	5.8	11.94	0.69	[64]
	15.0	11.5	1.73	[67]
	10.5	13.8	1.45	[67]
	11.0	12.5	1.38	[55]
	10.4	10.4	1.08	[51]
$Ti_3C_2F_2$	23.33	20.0	4.67	This work
$Ti_3C_2(OH)_2$	19.78	20.0	3.96	

structure that requires a high number of **k**-points to sample. By comparing the $\langle v^2 \rangle$ function of the different materials, we note that the addition of either surface termination to the Ti_3C_2 sheet results in an increase of the squared velocity density. This is due to the surface termination atoms pulling electrons off the central layer and lowering the Fermi level to intercept the highly dispersive Ti d-band along the M-K segment of the band structures.

Looking at the electronic scattering lifetimes $\tau_{n\mathbf{k}}$ shown in Fig. 4, we note that Ti_2CF_2, being the thinnest monosheet, also has the shortest lifetime. Among the terminated structures, $Ti_3C_2F_2$ and Ti_2CF_2 have shorter scattering lifetimes than $Ti_3C_2(OH)_2$, most likely due to the presence of flat bands near the Fermi level in the Γ–K region for the fluorinated structures. As a result, according to the SERTA calculation, $Ti_3C_2(OH)_2$ has the highest electrical conductivity. However, the full IBTE calculation reveals instead that $Ti_3C_2F_2$ has a higher electrical conductivity than $Ti_3C_2(OH)_2$ at temperatures up to 500 K.

H. Comparison with experiments

Several conductivity measurements of layered $Ti_3C_2T_x$ are reported with a variety of experimental setups [37,51–67]. The surface termination is either F or OH, but is generally unspecified. In practice, the bulk conductivity of MXene flakes depends on the synthesis method, which may yield different concentrations of defects and impurities, as well as different spacings between nanosheets.

From a dimensional analysis, the bulk conductivity must be proportional to the density of MXene nanosheets as $\sigma = \sigma_{2D}/L_z$, where σ_{2D} is the monolayer conductivity with units of Siemens (S) and L_z is the interlayer distance. In the present calculation, L_z is set arbitrarily to 20 Å, whereas in experiments L_z is inferred from x-ray diffraction (XRD) spectra.

Table II presents a list of recent experimental measurements of electrical conductivities. While the experimental precision is on the fourth significant digit or better, the measured values among different samples vary by an order of magnitude. The present calculation corresponds to a defect-free system, in which electron-phonon scattering is the only source of resistivity, and sets an upper bound on the conductivity. Comparing against the highest electrical conductivity achieved for $Ti_3C_2T_x$, the computed IBTE value at 300 K is indeed larger by 59% for $Ti_3C_2F_2$ and 34% for $Ti_3C_2(OH)_2$.

Aside from the **k**-points/**q**-points convergence, and unaccounted scattering channels like defects, other sources of error in our theoretical calculation include the thermal expansion of the lattice, the renormalization of the electron velocities due to phonons [49], as well as the accuracy of the exchange-correlation functional for the band structure [45] and the electron-phonon coupling strength [82–84]. Overall, an overestimation by about 50% represents a reasonably good agreement, and an accuracy comparable to that of typical mobility calculations in 2D materials [47].

III. CONCLUSION

In summary, we performed a comparative study of the electronic transport of the pristine Ti_3C_2, terminated $Ti_3C_2T_2$ ($T = $ F, OH), and Ti_2CF_2 monosheets from first principles. We computed the electrical conductivity of the MXenes with different relaxation time approximations, as well as with the iterative Boltzmann transport equation. We found that the SERTA underestimates the conductivity, while the MRTA is in better agreement with the IBTE. However, the relative differences among monosheets with different surface terminations can only be resolved by the iterative procedure. Nonetheless, the relaxation-time approximation provides a useful understanding of the underlying physics by decomposing the electrical conductivity into scattering lifetime and squared velocity density. The computed monolayer conductivities underestimate the experimentally measured values by 30%–60%, a reasonable agreement given that the conductivity may vary by orders of magnitude depending on the structural details of the materials. The methodology presented in this work may thus be used to further explore the conductivity of 2D compounds and identify candidate materials for energy storage.

[1] J.-C. Lei, X. Zhang, and Z. Zhou, Front. Phys. **10**, 276 (2015).

[2] B. Anasori, M. R. Lukatskaya, and Y. Gogotsi, Nat. Rev. Mater. **2**, 16098 (2017).

[3] M. Naguib, M. Kurtoglu, V. Presser, J. Lu, J. Niu, M. Heon, L. Hultman, Y. Gogotsi, and M. W. Barsoum, Adv. Mater. **23**, 4248 (2011).

[4] M. Naguib, O. Mashtalir, J. Carle, V. Presser, J. Lu, L. Hultman, Y. Gogotsi, and M. W. Barsoum, ACS Nano **6**, 1322 (2012).

[5] A. N. Enyashin and A. L. Ivanovskii, J. Phys. Chem. C **117**, 13637 (2013).

[6] Z. Liu and H. N. Alshareef, Adv. Electron. Mater. **7**, 2100295 (2021).

[7] M. Naguib, M. W. Barsoum, and Y. Gogotsi, Adv. Mater. **33**, 2103393 (2021).

[8] M. Khazaei, A. Mishra, N. S. Venkataramanan, A. K. Singh, and S. Yunoki, Curr. Opin. Solid State Mater. Sci. **23**, 164 (2019).

[9] S. Sun, C. Liao, A. M. Hafez, H. Zhu, and S. Wu, Chem. Eng. J. **338**, 27 (2018).

[10] U. Yorulmaz, A. Özden, N. K. Perkgöz, F. Ay, and C. Sevik, Nanotechnology **27**, 335702 (2016).

[11] Y. Xie, M. Naguib, V. N. Mochalin, M. W. Barsoum, Y. Gogotsi, X. Yu, K.-W. Nam, X.-Q. Yang, A. I. Kolesnikov, and P. R. C. Kent, J. Am. Chem. Soc. **136**, 6385 (2014).

[12] D. Er, J. Li, M. Naguib, Y. Gogotsi, and V. B. Shenoy, ACS Appl. Mater. Interfaces **6**, 11173 (2014).

[13] Y. Sun, D. Chen, and Z. Liang, Mater. Today Energy **5**, 22 (2017).

[14] Q. Shan, X. Mu, M. Alhabeb, C. E. Shuck, D. Pang, X. Zhao, X.-F. Chu, Y. Wei, F. Du, G. Chen, Y. Gogotsi, Y. Gao, and Y. Dall'Agnese, Electrochem. Commun. **96**, 103 (2018).

[15] R. B. Rakhi, B. Ahmed, M. N. Hedhili, D. H. Anjum, and H. N. Alshareef, Chem. Mater. **27**, 5314 (2015).

[16] M. Ghidiu, M. R. Lukatskaya, M.-Q. Zhao, Y. Gogotsi, and M. W. Barsoum, Nature (London) **516**, 78 (2014).

[17] M. Naguib, V. N. Mochalin, M. W. Barsoum, and Y. Gogotsi, Adv. Mater. **26**, 992 (2014).

[18] M. Naguib, J. Come, B. Dyatkin, V. Presser, P.-L. Taberna, P. Simon, M. W. Barsoum, and Y. Gogotsi, Electrochem. Commun. **16**, 61 (2012).

[19] M. Naguib, J. Halim, J. Lu, K. M. Cook, L. Hultman, Y. Gogotsi, and M. W. Barsoum, J. Am. Chem. Soc. **135**, 15966 (2013).

[20] Y. Ding, J. Zhang, A. Guan, Q. Wang, S. Li, A. M. Al-Enizi, L. Qian, L. Zhang, and G. Zheng, Nano Convergence **8**, 14 (2021).

[21] X. Xie and N. Zhang, Adv. Funct. Mater. **30**, 2002528 (2020).

[22] A. D. Handoko, S. N. Steinmann, and Z. W. Seh, Nanoscale Horiz. **4**, 809 (2019).

[23] M. R. Lukatskaya, B. Dunn, and Y. Gogotsi, Nat. Commun. **7**, 12647 (2016).

[24] Q. Hu, D. Sun, Q. Wu, H. Wang, L. Wang, B. Liu, A. Zhou, and J. He, J. Phys. Chem. A **117**, 14253 (2013).

[25] D. Tian, S. R. Denny, K. Li, H. Wang, S. Kattel, and J. G. Chen, Chem. Soc. Rev. **50**, 12338 (2021).

[26] X. Yang, Y. Zhang, Z. Fu, Z. Lu, X. Zhang, Y. Wang, Z. Yang, and R. Wu, ACS Appl. Mater. Interfaces **12**, 28206 (2020).

[27] X. Zou, H. Liu, H. Xu, X. Wu, X. Han, J. Kang, and K. M. Reddy, Mater. Today Energy **20**, 100668 (2021).

[28] Y.-W. Cheng, J.-H. Dai, Y.-M. Zhang, and Y. Song, J. Phys. Chem. C **122**, 28113 (2018).

[29] H. Tang, Q. Hu, M. Zheng, Y. Chi, X. Qin, H. Pang, and Q. Xu, Prog. Nat. Sci.: Mater. Int. **28**, 133 (2018).

[30] M. Hu, H. Zhang, T. Hu, B. Fan, X. Wang, and Z. Li, Chem. Soc. Rev. **49**, 6666 (2020).

[31] D. Wang, Y. Gao, Y. Liu, Y. Gogotsi, X. Meng, G. Chen, and Y. Wei, J. Mater. Chem. A **5**, 24720 (2017).

[32] O. Mashtalir, M. Naguib, V. N. Mochalin, Y. Dall'Agnese, M. Heon, M. W. Barsoum, and Y. Gogotsi, Nat. Commun. **4**, 1716 (2013).

[33] H. Wang, Y. Wu, J. Zhang, G. Li, H. Huang, X. Zhang, and Q. Jiang, Mater. Lett. **160**, 537 (2015).

[34] P. Eklund, M. Beckers, U. Jansson, H. Högberg, and L. Hultman, Thin Solid Films **518**, 1851 (2010).

[35] M. Khazaei, A. Ranjbar, Y. Liang, and S. Yunoki, in *2D Metal Carbides and Nitrides (MXenes)*, edited by B. Anasori and Y. Gogotsi (Springer International Publishing, Cham, 2019), pp. 255–289.

[36] M. Khazaei, A. Ranjbar, M. Arai, T. Sasaki, and S. Yunoki, J. Mater. Chem. C **5**, 2488 (2017).

[37] J. Halim, M. R. Lukatskaya, K. M. Cook, J. Lu, C. R. Smith, L.-Å. Näslund, S. J. May, L. Hultman, Y. Gogotsi, P. Eklund, and M. W. Barsoum, Chem. Mater. **26**, 2374 (2014).

[38] C. Sevik, J. Bekaert, and M. V. Milosevic, Nanoscale **15**, 8792 (2023).

[39] T. Schultz, N. C. Frey, K. Hantanasirisakul, S. Park, S. J. May, V. B. Shenoy, Y. Gogotsi, and N. Koch, Chem. Mater. **31**, 6590 (2019).

[40] A. N. Gandi, H. N. Alshareef, and U. Schwingenschlögl, Chem. Mater. **28**, 1647 (2016).

[41] A. Champagne, L. Shi, T. Ouisse, B. Hackens, and J.-C. Charlier, Phys. Rev. B **97**, 115439 (2018).

[42] S. Das Sarma, S. Adam, E. H. Hwang, and E. Rossi, Rev. Mod. Phys. **83**, 407 (2011).

[43] T.-H. Liu, J. Zhou, B. Liao, D. J. Singh, and G. Chen, Phys. Rev. B **95**, 075206 (2017).

[44] S. Poncé, D. Jena, and F. Giustino, Phys. Rev. B **100**, 085204 (2019).

[45] S. Poncé, E. R. Margine, and F. Giustino, Phys. Rev. B **97**, 121201(R) (2018).

[46] W. Li, Phys. Rev. B **92**, 075405 (2015).

[47] S. Poncé, W. Li, S. Reichardt, and F. Giustino, Rep. Prog. Phys. **83**, 036501 (2020).

[48] G. Brunin, H. P. C. Miranda, M. Giantomassi, M. Royo, M. Stengel, M. J. Verstraete, X. Gonze, G.-M. Rignanese, and G. Hautier, Phys. Rev. B **102**, 094308 (2020).

[49] F. Brown-Altvater, G. Antonius, T. Rangel, M. Giantomassi, C. Draxl, X. Gonze, S. G. Louie, and J. B. Neaton, Phys. Rev. B **101**, 165102 (2020).

[50] R. Claes, G. Brunin, M. Giantomassi, G.-M. Rignanese, and G. Hautier, Phys. Rev. B **106**, 094302 (2022).

[51] H. Chen, Y. Wen, Y. Qi, Q. Zhao, L. Qu, and C. Li, Adv. Funct. Mater. **30**, 1906996 (2020).

[52] D. H. Ho, Y. Y. Choi, S. B. Jo, J.-M. Myoung, and J. H. Cho, Adv. Mater. **33**, 2005846 (2021).

[53] A. Iqbal, J. Kwon, M.-K. Kim, and C. Koo, Mater. Today Adv. **9**, 100124 (2021).

[54] Z. Ling, C. E. Ren, M.-Q. Zhao, J. Yang, J. M. Giammarco, J. Qiu, M. W. Barsoum, and Y. Gogotsi, Proc. Natl. Acad. Sci. USA **111**, 16676 (2014).

[55] A. Lipatov, A. Goad, M. J. Loes, N. S. Vorobeva, J. Abourahma, Y. Gogotsi, and A. Sinitskii, Matter **4**, 1413 (2021).

[56] C. Li, S. Kota, C. Hu, and M. W. Barsoum, J. Ceram. Sci. Technol. **7**, 301 (2016).

[57] T. S. Mathis, K. Maleski, A. Goad, A. Sarycheva, M. Anayee, A. C. Foucher, K. Hantanasirisakul, C. E. Shuck, E. A. Stach, and Y. Gogotsi, ACS Nano **15**, 6420 (2021).

[58] A. Miranda, J. Halim, M. W. Barsoum, and A. Lorke, Appl. Phys. Lett. **108**, 033102 (2016).

[59] S. A. Mirkhani, A. Shayesteh Zeraati, E. Aliabadian, M. Naguib, and U. Sundararaj, ACS Appl. Mater. Interfaces **11**, 18599 (2019).

[60] C. Qiao, H. Wu, X. Xu, Z. Guan, and W. Ou-Yang, Adv. Mater. Interfaces **8**, 2100903 (2021).

[61] A. Sarycheva, A. Polemi, Y. Liu, K. Dandekar, B. Anasori, and Y. Gogotsi, Sci. Adv. **4**, eaau0920 (2018).

[62] F. Shahzad, A. Iqbal, H. Kim, and C. M. Koo, Adv. Mater. **32**, 2002159 (2020).

[63] F. Shahzad, M. Alhabeb, C. B. Hatter, B. Anasori, S. Man Hong, C. M. Koo, and Y. Gogotsi, Science **353**, 1137 (2016).

[64] A. Shayesteh Zeraati, S. A. Mirkhani, P. Sun, M. Naguib, P. V. Braun, and U. Sundararaj, Nanoscale **13**, 3572 (2021).

[65] P. Song, B. Liu, H. Qiu, X. Shi, D. Cao, and J. Gu, Compos. Commun. **24**, 100653 (2021).

[66] J. Tang, X. Huang, T. Qiu, X. Peng, T. Wu, L. Wang, B. Luo, and L. Wang, Chem.-Eur. J. **27**, 1921 (2021).

[67] J. Zhang, N. Kong, S. Uzun, A. Levitt, S. Seyedin, P. A. Lynch, S. Qin, M. Han, W. Yang, J. Liu, X. Wang, Y. Gogotsi, and J. M. Razal, Adv. Mater. **32**, 2001093 (2020).

[68] X. Gonze, B. Amadon, P.-M. Anglade, J.-M. Beuken, F. Bottin, P. Boulanger, F. Bruneval, D. Caliste, R. Caracas, M. Côté, T. Deutsch, L. Genovese, P. Ghosez, M. Giantomassi, S. Goedecker, D. Hamann, P. Hermet, F. Jollet, G. Jomard, S. Leroux *et al.*, Comput. Phys. Commun. **180**, 2582 (2009).

[69] X. Gonze, B. Amadon, G. Antonius, F. Arnardi, L. Baguet, J.-M. Beuken, J. Bieder, F. Bottin, J. Bouchet, E. Bousquet, N. Brouwer, F. Bruneval, G. Brunin, T. Cavignac, J.-B. Charraud, W. Chen, M. Côté, S. Cottenier, J. Denier, G. Geneste *et al.*, Comput. Phys. Commun. **248**, 107042 (2020).

[70] J. P. Perdew, K. Burke, and M. Ernzerhof, Phys. Rev. Lett. **77**, 3865 (1996).

[71] M. van Setten, M. Giantomassi, E. Bousquet, M. Verstraete, D. Hamann, X. Gonze, and G.-M. Rignanese, Comput. Phys. Commun. **226**, 39 (2018).

[72] Y. Bai, K. Zhou, N. Srikanth, J. H. L. Pang, X. He, and R. Wang, RSC Adv. **6**, 35731 (2016).

[73] T. Hu, J. Wang, H. Zhang, Z. Li, M. Hu, and X. Wang, Phys. Chem. Chem. Phys. **17**, 9997 (2015).

[74] Q. Tang, Z. Zhou, and P. Shen, J. Am. Chem. Soc. **134**, 16909 (2012).

[75] S. Wang, J.-X. Li, Y.-L. Du, and C. Cui, Comput. Mater. Sci. **83**, 290 (2014).

[76] M. Khazaei, M. Arai, T. Sasaki, A. Ranjbar, Y. Liang, and S. Yunoki, Phys. Rev. B **92**, 075411 (2015).

[77] H. Gholivand, S. Fuladi, Z. Hemmat, A. Salehi-Khojin, and F. Khalili-Araghi, J. Appl. Phys. **126**, 065101 (2019).

[78] F. Giustino, Rev. Mod. Phys. **89**, 015003 (2017).

[79] S. Wen, J. Ma, A. Kundu, and W. Li, Phys. Rev. B **102**, 064303 (2020).

[80] D. G. Shankland, Int. J. Quantum Chem. **5**, 497 (2009).

[81] D. Koelling and J. Wood, J. Comput. Phys. **67**, 253 (1986).

[82] G. Antonius, S. Poncé, P. Boulanger, M. Côté, and X. Gonze, Phys. Rev. Lett. **112**, 215501 (2014).

[83] F. Karsai, M. Engel, G. Kresse, and E. Flage-Larsen, New J. Phys. **20**, 123008 (2018).

[84] Z. Li, G. Antonius, M. Wu, F. H. da Jornada, and S. G. Louie, Phys. Rev. Lett. **122**, 186402 (2019).